A Universal Approximation for Conductance Blockade in Thin Nanopore Membranes

Arjav Shah, Shakul Pathak, Kun Li, Slaven Garaj, Martin Z. Bazant, Ankur Gupta, and Patrick S. Doyle*

ACCESS | Metrics & More | Article Recommendations | Supporting Information

ABSTRACT: Nanopore-based sensing platforms have transformed single-molecule detection and analysis. The foundation of nanopore translocation experiments lies in conductance measurements, yet existing models, which are largely phenomenological, are inaccurate in critical experimental conditions such as thin and tightly fitting pores. Of the two components of the conductance blockade, channel and access resistance, the access resistance is poorly modeled. We present a comprehensive investigation of the access resistance and associated conductance blockade in thin nanopore membranes. By combining a first-principles approach, multiscale modeling, and experimental validation, we propose a unified theoretical modeling framework. The analytical model derived as a result surpasses current approaches across a broad parameter range. Beyond advancing our theoretical understanding, our framework's versatility enables analyte size inference and predictive insights into conductance blockade behavior. Our results will facilitate the design and optimization of nanopore devices for diverse applications, including nanopore base calling and data storage.

KEYWORDS: access resistance, electrostatics, conductance, 2D materials, nanopores
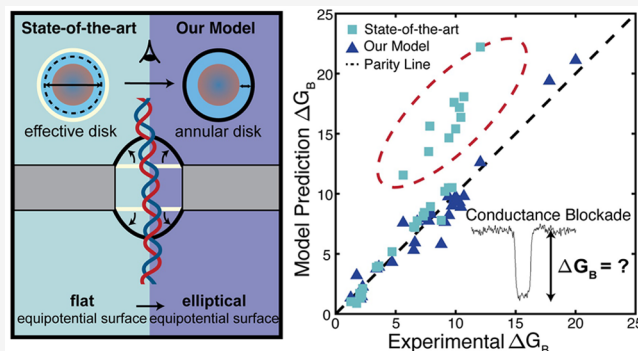
Nanopores have evolved as valuable single-molecule analytical tools over the past four decades.[1,2] While ubiquitous in nucleic acid sequencing applications, the utilization of nanopores extends into broader molecule sensing, biomolecule characterization, catalysis, desalination, and power generation.[2−7] The technology has been widely exploited for the detection, fingerprinting, and sequencing of biomolecules for advances in medicine, biotechnology, and forensics. In particular, it has been extensively used to probe the mechanics and dynamics of DNA, including double-stranded DNA (dsDNA)[1] and DNA knots,[8−10] proteomics,[11−13] virology,[14−17] etc.

Mapping the experimental observables to their associated analyte characteristics is a critical enabler for nanopore sensing in diverse applications. Conductance measurement is the cornerstone of nanopore translocation experiments. A baseline open current exists due to the electrophoretic movement of ions through a pore in an otherwise insulating free-standing membrane (Figure 1a). The presence of an analyte inside the pore impedes the flow of ions. As a result, the translocation of a charged analyte through the pore under the influence of an electric field causes a transient change in the electrical resistance of the system (Figure 1b). On the basis of the principle of resistive pulse sensing, the change in resistance manifests as a modulation in the ionic current in current−time pulse signatures in experiments (Figure 1c).[18] The nanopore system is ultrasensitive to these changes in the ionic current

such that the electrical signatures encompass information about the morphological characteristics of translocating analytes. For instance, the amplitude of a signature pulse, known as current blockade ΔI_B, encodes analyte width (or thickness) information, which is important for molecule characterization and fingerprinting applications. Normalized ΔI_B is termed conductance blockade ΔG_B (Figure 1c). An accurate, physics-based model of ΔG_B is critical for the interpretation of experimental observables.

Long, rod-like, charged cylindrical objects such as dsDNA, filamentous viruses such as *fd* or TMV, nanorods, and DNA nanostructures such as DNA origami bundles, etc. (Figure 1d), have been studied extensively because of their importance in applications such as sequencing, diagnostics, and biophysical studies.[15,16,19−22] In addition to the prevalence of such analytes, their cylindrical symmetry offers mathematical convenience for the use of cylindrical or oblate spheroidal coordinate systems in analytical conductance models. Relevant length scales for a system with cylindrical analytes including
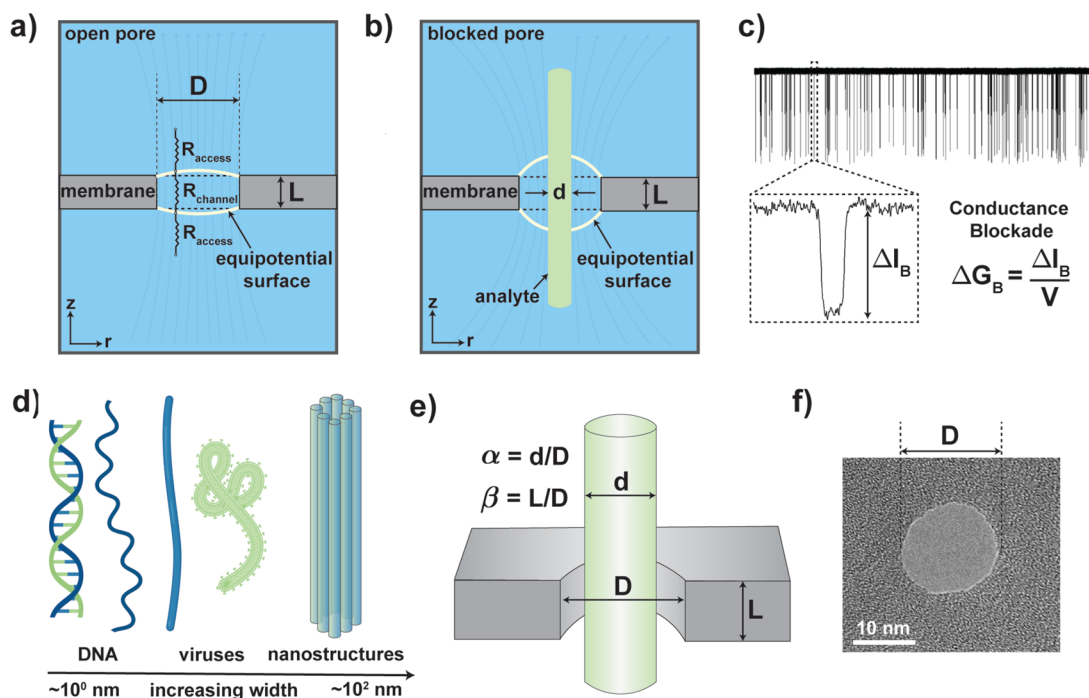
Figure 1. State of the nanopore system corresponding to the changes in the curvature of the equipotential surface for (a) an open pore shown with minimal circuit representation of the system and (b) a blocked pore in the presence of a long, cylindrical analyte. (c) Representative resistive pulse outputs from experiments with amplitude current blockade ΔI_B. (d) Analytes of interest such as DNA, viruses, and nanostructures. (e) Dimensionless groups in the system, α (analyte:pore diameter ratio) $\in [0, 1)$ and β (pore aspect ratio) $\in (0, 5)$ typically. (f) Transmission electron microscopy image of a silicon nitride SiN_x pore used for detection.
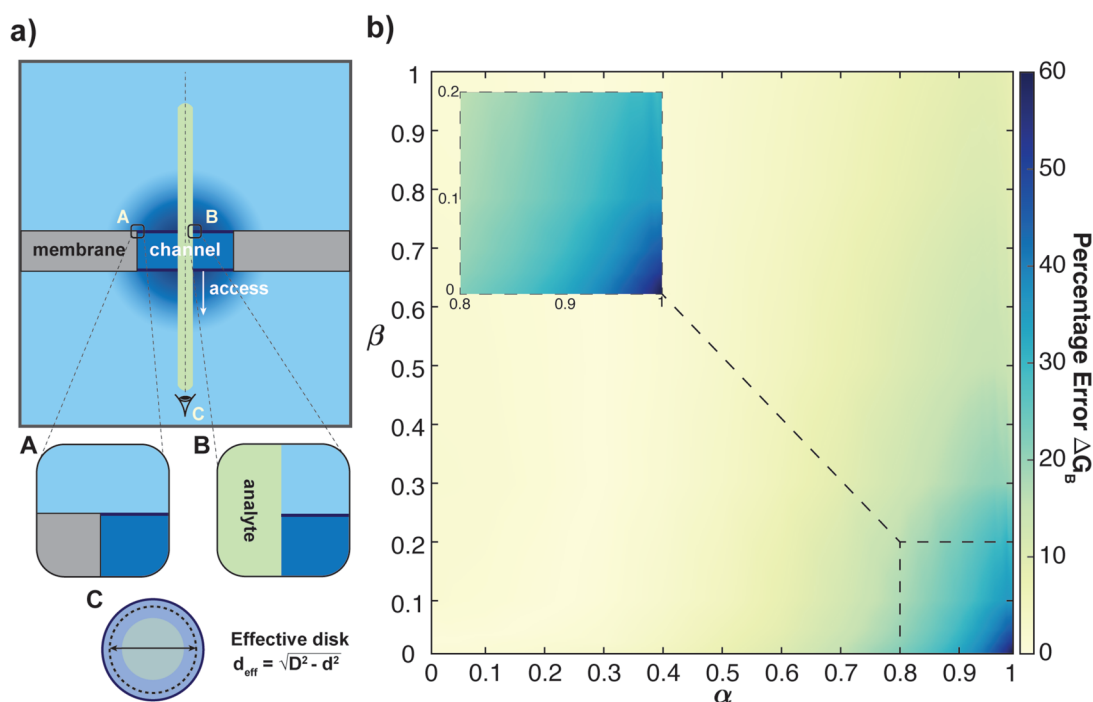

Figure 2. Kowalczyk model. (a) System partitioning into channel and access regions based on a flat equipotential surface (highlighted in parts A and B) that is treated as an effective disk shown in part C. (b) Heat map of the relative error in conductance blockade ΔG_B compared to fully coupled, continuum simulations. The inset highlights the parameter space with significantly high errors in ΔG_B of ≤60%.

pore diameter D, membrane thickness L, and analyte diameter d are depicted in panels e and f of Figure 1. Analyte length l does not play a role in modulating ΔG_B as long as $l \gg L$. On the basis of these three length scales, two dimensionless groups are defined in the system: $\alpha = d/D$ represents how loosely/

tightly fit the analyte is inside the pore, and $\beta = L/D$ is the pore aspect ratio (Figure 1e).

The total conductance of the nanopore system is determined by the sum of key resistances in series that include the access (or convergence) and channel (or pore) resistances. The
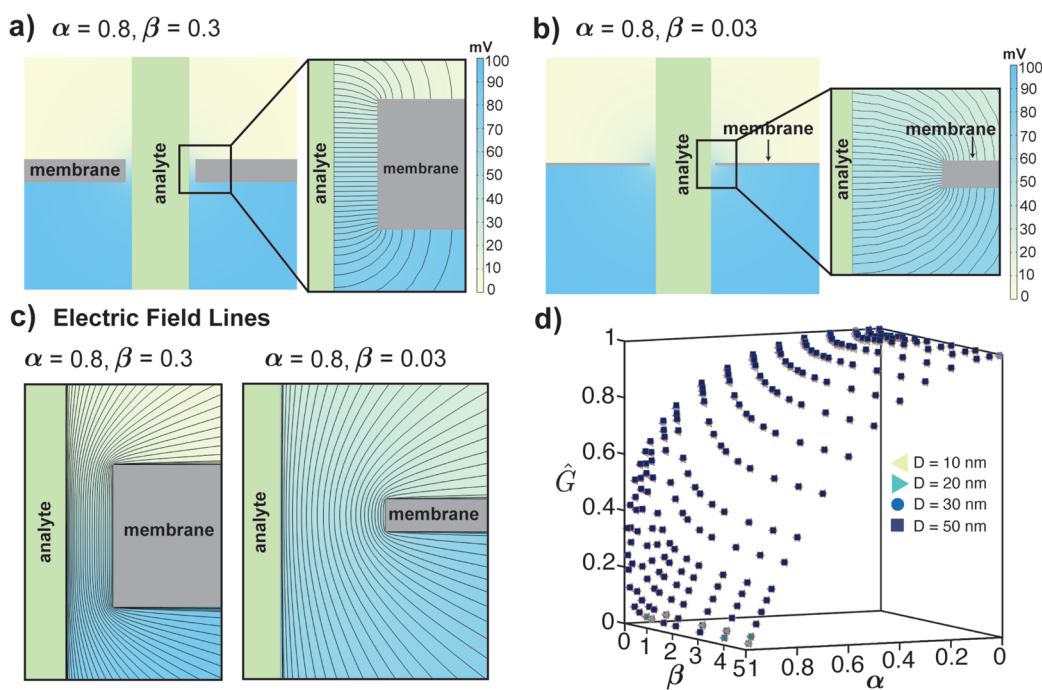
Figure 3. Continuum simulations. (a and b) Electric potential gradient and equipotential surfaces (enlarged) for thick and thin pores, respectively. (c) Bending of electric field lines around the pore mouth. (d) Variation of dimensionless conductance blockade (equation S9) over $\alpha-\beta$ space shown for various D values.

resistance to the flow of ions inside the pore channel is termed the channel resistance, $R_{channel}$. The potential gradient across the bulk electrolyte solution due to the distortion and convergence of electric field lines around the pore mouths is approximated by the access resistance, R_{access}, which is equivalent to entrance effects in the flow of a fluid through constrictions. Existing conductance models have been primarily developed for long, cylindrical analytes.[23−25] While these models work well for small α and $\beta \gg 1$, they fail for thin membranes ($\beta \ll 1$). However, with the advent of and progress in two-dimensional materials, the increasing use of extremely thin membranes for nanopore experiments is imperative. These are ideal for high-resolution, high-throughput nanopore-based single-molecule detection. They have been reported to have several advantages in terms of manufacturability, signal-to-noise ratio (SNR), electrical sensitivity, and stability.[26,27] In addition, tightly fitted pores ($\alpha \rightarrow 1$) are critical for high experimental sensitivity and SNR.[27] As a result, accurate models for conductance in thin and tightly fitted pores, i.e., ΔG_B for $\alpha \rightarrow 1$ and $\beta \ll 1$, are critical.

A key component of ΔG_B, R_{access} dominates for thin pores [$R_{access}/R_{channel} \sim 1/\beta$ (see the Supporting Information)]. On the basis of the literature, it is widely understood that R_{access} for an open pore depends on only the resistivity of the conducting medium and pore diameter D.[28−30] However, a comprehensive understanding of the perturbation in R_{access} in the presence of an analyte inside the pore remains elusive. First-generation models for R_{access}, proposed by Hall and Hille, have been developed for ion channels in pharmacological applications, primarily dealing with open pore scenarios ($\alpha = 0$).[29,30] The presence of an analyte has only been phenomenologically or empirically accounted for thus far, including in more recent models by Kowalczyk[23] and Carlsen.[24] The most widely used model is that of Kowalczyk, which combines R_{access} from Hall[30]

and $R_{channel}$ from ohm's law integrated across the channel. The presence of an analyte is captured on the basis of an effective pore diameter that is exact for $R_{channel}$ but is only a first-order approximation for R_{access} (Figure 2a). The Carlsen model overcorrects the Kowalczyk model by accounting for the analyte as an added negative access conductance in addition to the effective pore diameter.[24]

The most important assumption in Hall's approach is that the equipotential surface at the pore mouth is a planar disk (Figure 2a, parts A and B). While this assumption is suitable for an open pore, it breaks down for tightly fitted pores. For an open pore, a large fraction of electric field lines can pass straight through the pore unhindered. In contrast, in the presence of an analyte, the field lines are no longer straight in the pore channel and bend significantly around the pore mouth as they exit. As a result, the equipotential surface at the pore mouth cannot be a flat disk as assumed in the model because it has to remain perpendicular to the field lines. Moreover, in the presence of an analyte, the pore is no longer "open" and thus no longer a complete disk (Figure 2a, part C).

To overcome the assumptions of the existing models, we use fully coupled simulations of the Poisson−Nernst−Planck and Navier−Stokes equations with appropriate boundary conditions in *COMSOL Multiphysics*. We show that the state-of-the-art approaches perform poorly in the critical experimental limits ($\alpha \rightarrow 1$, $\beta \ll 1$). The heat map in Figure 2b depicts the relative error in the prediction of ΔG_B using the Kowalczyk model when compared to the simulation results. The errors of the Kowalczyk model are as high as 60% for thin and tightly fitted pores ($\alpha \rightarrow 1$, $\beta \ll 1$). Unsurprisingly, these are the cases farthest from open pore scenarios in which the flat disk assumption is not justified. This limits the usage of the existing models in current applications.[25]

We hypothesize that an annular disk is a better approximation than an effective disk, and that the equipotential
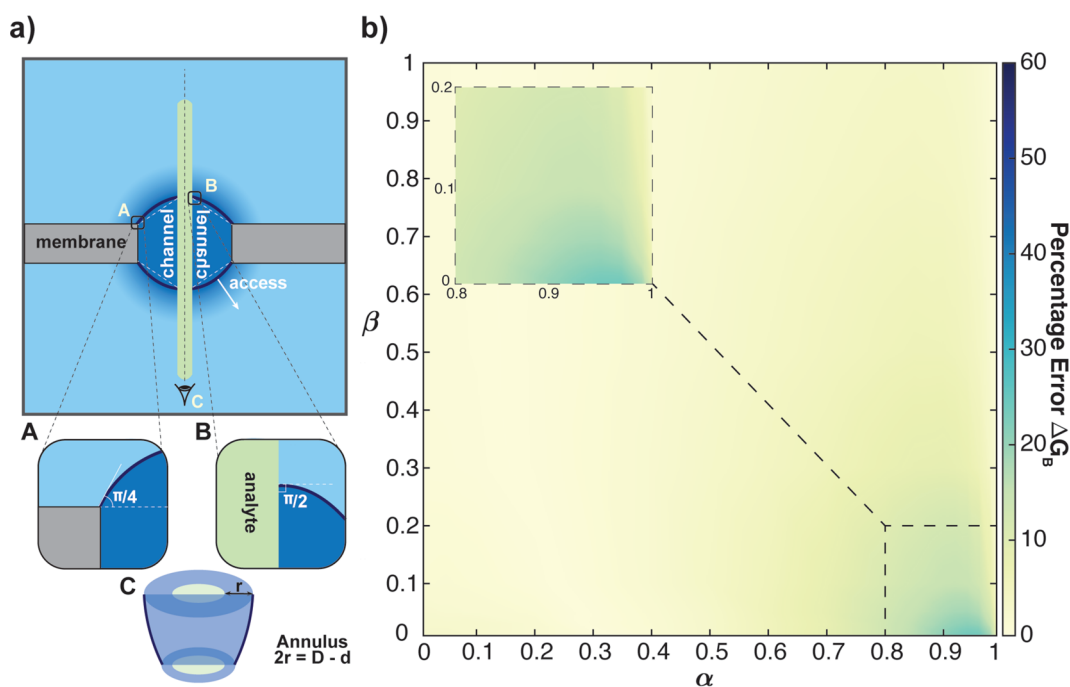
Figure 4. Our model. (a) Updated system partitioning into channel and access regions based on the equipotential surface (highlighted in parts A and B) that forms a truncated elliptical cone with an annular region shown in part C. (b) Heat map of the relative error in conductance blockade ΔG_B as compared to fully coupled, continuum simulations. The inset emphasizes the significant reduction in errors in ΔG_B for an important parameter range.

surface is an elliptical arc, drawing inspiration from analogous heat and mass transport problems.[31,32] The access region and, hence, its associated resistance, R_{access}, is perturbed nontrivially during the translocation of an analyte through the region. To test our hypotheses, we use a combination of simulations, analytical modeling, and experimental validation to elucidate the role of the access region in determining ΔG_B in the presence of cylindrical analytes, particularly for thin pores.

The equipotential surface at the pore mouth is curved (Figure 3a,b) because the fraction of electric field lines that bend for thin membranes and tightly fitted pores is very high (Figure 3c). As a result, the assumption of a planar disk at the pore mouth is a poor approximation in this limit and influences the accuracy of the existing R_{access} models. In addition, due to the assumption of a hyperbolic shape of the analyte (specifically dsDNA) in the pore instead of a cylinder, the Kowalczyk model consistently overestimates ΔG_B.

Toward proposing a new modeling framework and the development of a more accurate analytical conductance model, we show that two dimensionless groups, α and β, are sufficient to predict the conductance of a nanopore system; i.e., if two systems have the same (α, β), they will have the same nondimensional conductance, $\hat{G} = G_{B,total}/G_{O,channel}$ (eq S9), where $G_{O,channel}$ and $G_{B,total}$ refer to the open channel and total blocked pore conductances, respectively. This is evident by a collapse of data points with the same (α, β) values over the entire parameter space in Figure 3d. Leveraging this insight, we propose and validate a universal, physics-inspired analytical model for ΔG_B, demonstrating superior performance compared to the existing models for a wide parameter range. We present a modeling framework with three key novel features: (1) accurate estimation for the capacitance of an annular disc and, hence, R_{access} dominant for thin pores, (2) nonhyperbolic, cylindrical analyte shapes, and (3) incorporation of electric

field bending and, hence, the dependence of channel and access region partitions on both α and β.

Consider a long, cylindrical analyte of diameter d with length l long enough to pierce both the access regions of a nanopore of diameter D and thickness L. We focus on concentrated electrolyte systems, and any double-layer effects can be neglected to first order (Debye length, $\lambda_{DL}/D \ll 1$ and $\lambda_{DL}/d \ll 1$). Therefore, any surface charge on the analyte or pore is screened by a thin double layer. Low-molarity approximation is beyond the scope of this paper; charge- and flow-related effects such as electro-osmotic flow, conductivity enhancement, double-layer overlap, etc., have been ignored. While λ_{DL} could be comparable to the gap $(D - d)$ at high salt concentrations, unlike predicted by the Debye–Huckel theory, exact ion concentration profiles are not critical to the calculations of integrated quantities like capacitance or conductance, particularly for salts with comparable anionic and cationic mobilities.[33−35] At the pore length scale, the analyte and pore surfaces can be assumed to act like an insulator in a background electric field. Charge screening in the pore results in field lines running parallel to the pore wall and analyte surface (Figure 3c). The geometric boundaries between the channel and access region can now be assigned by noting that the equipotential line that passes through the corner of the pore wall (Figure 4a, part A) is incident on the corner at an angle of 45° (see the Supporting Information).[36] Because the analyte surface has no net charge at high ionic strengths, the equipotential lines are incident perpendicular to its surface (Figure 4a, part B).

Similar to Hall's approach, we seek to find the capacitance of the equipotential surface sketched in Figure 4a.[30] As a first-order approximation, we consider the equipotential surface as a flat punctured disk surface of inner diameter d and outer diameter D, although it is a surface of revolution of an elliptic
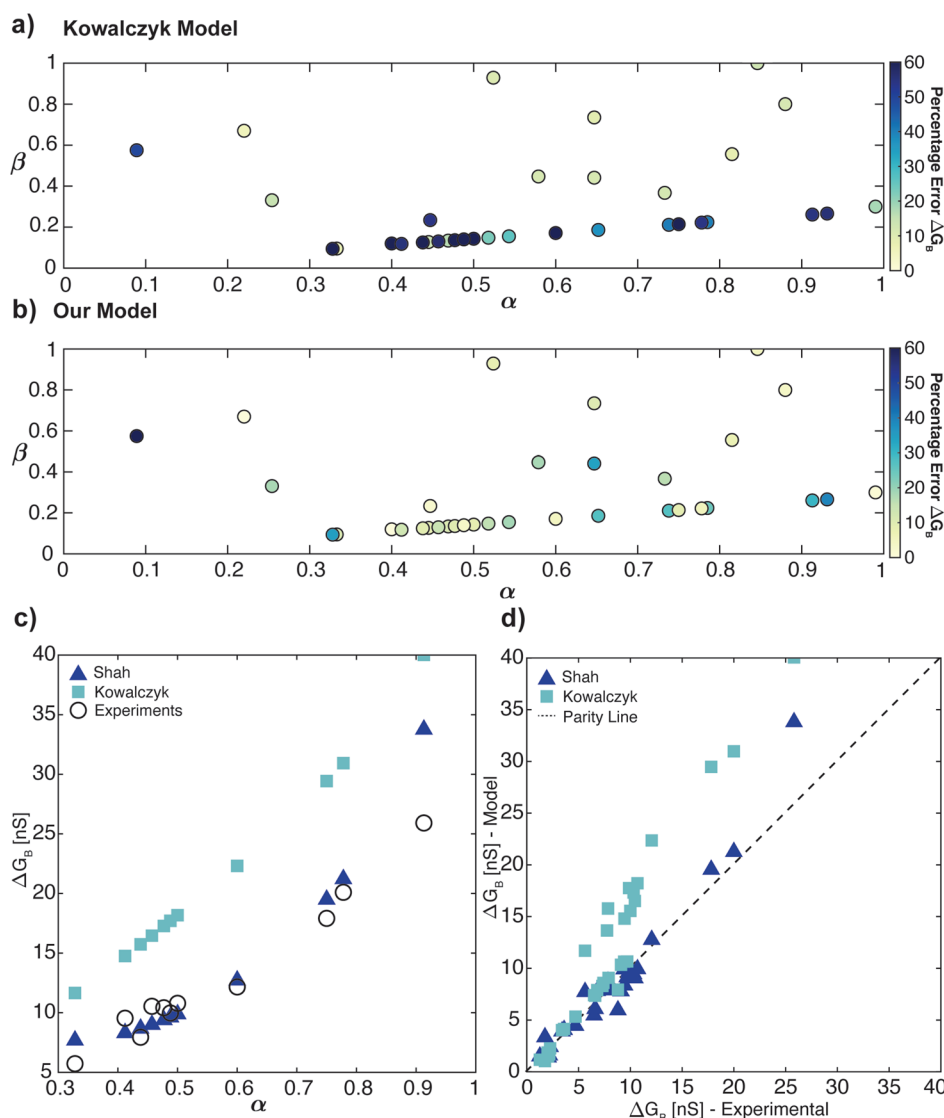
Figure 5. Experimental validation. Comparison of relative errors in conductance blockade ΔG_B estimates from (a) Kowalczyk's model and (b) our model (Shah) with respect to experiments.[39−45] (c) Comparison of absolute ΔG_B values for $\beta \sim 0.2$ for our model, Kowalczyk's model, and experiments. (d) Parity plot comparing the model results with experimental data, highlighting the superior performance of the our proposed model over the state-of-the-art conductance model.

arc.[32] To estimate the capacitance, we utilize the work of Smythe who proposed an iterative method for this problem, starting with the charge distribution of an equipotential disk (see the Supporting Information).[37] These calculations yield

$$\frac{C_{\text{annulus}}}{C_{\text{disk}}} = \frac{2}{\pi}[\cos^{-1}\alpha + (1 - \alpha^2)^{1/2}\tanh^{-1}\alpha]$$
$$\times \left[1 + \left(\frac{0.0143}{\alpha}\right)\tan^3(1.28\alpha)\right] \tag{1}$$

where C_{annulus} and C_{disk} are the capacitances of the flat annulus and disk, respectively. For $\alpha \to 0$, we determine that the values are equal. Hereafter, we refer to the open and blocked pore conductances as $G_{O,i}$ and $G_{B,i}$, respectively, such that i $\in$ {total, access, channel}. To obtain the desired quantity $G_{B,\text{access}}$, we invoke that the conductance is proportional to the capacitance because solving for the two problems is mathematically equivalent[38] ($G = C\sigma/\varepsilon$, where σ and ε are the electrolyte

conductivity and permittivity of free space, respectively) and hence

$$\frac{G_{B,\text{access}}}{G_{O,\text{access}}} = \frac{2}{\pi}[\cos^{-1}\alpha + (1 - \alpha^2)^{1/2}\tanh^{-1}\alpha]$$
$$\times \left[1 + \left(\frac{0.0143}{\alpha}\right)\tan^3(1.28\alpha)\right] \tag{2}$$

The other contribution to the total conductance, $G_{B,\text{channel}}$, is identical to the previous approaches for the flat punctured disk surface:

$$G_{B,\text{channel}} = \frac{\pi\sigma D}{4\beta}(1 - \alpha^2) \tag{3}$$

Conductance blockade ΔG_B can be obtained by subtracting the total blocked conductance from the open conductance:

$$\Delta G_B = G_{O,total} - G_{B,total} = \sigma D \left(\frac{4\beta}{\pi} + 1 \right)^{-1}$$

$$- \left(G_{B,channel}^{-1} + G_{B,access}^{-1} \right)^{-1} \tag{4}$$

As a second-order approximation, the equipotential surface is now assumed to be an inclined annular disk because the equipotential surface that passes through the corner of the pore is curved (Figure 3b,c). Assuming a partitioning scheme in which the boundary between the access and channel region is given by a straight line inclined at an angle θ with the horizontal, instead of fixing it at 45° as previously discussed (Figure 4a), yields an improved estimate for an appropriately fitted value of parameter θ (second-order correction), such that θ is the only phenomenological parameter. The updated model for $G_{B,access}$ reads (see the Supporting Information)

$$G_{B,access} = \frac{\sec \theta \sigma}{\varepsilon} C_{annulus} \tag{5}$$

Proceeding in manner similar to that of eq 3, we obtain eq 6 (see the Supporting Information). It is noteworthy that our proposed model (eqs 5 and 6) converges to the traditional model in the limits of open, thick pore cases, i.e., $\alpha \to 0, \beta \gg 1$ (see the Supporting Information).

$$G_{B,channel} = \frac{\pi \sigma D}{2 \sin \theta} \left\{ -(1 - \alpha) + \left(1 + \frac{\beta}{\tan \theta} \right) \right.$$

$$\left. \times \ln \left[1 + \frac{\tan \theta}{\beta}(1 - \alpha) \right] \right\} \tag{6}$$

We systematically evaluate the model performance (eqs 4−6) against simulation results for a wide range of parameters: $\alpha \in [0, 0.99]$ and $\beta \in [0.03, 5]$ for $D \in [10, 50]$ nm (equating to 867 unique cases). Figure 4b shows the relative error in ΔG_B estimated using our newly proposed model, which upon comparison with Figure 2b, clearly underscores that our new model significantly outperforms the state-of-the-art model in the thin and tightly fitted pore limit, i.e., small β and large α. When all cases with $\beta \leq 0.1$ are combined, the average errors are 9% and 18% and the maximum errors are 24% and 61% for our model and Kowalczyk's model, respectively (Table S2). Additional analyses and comparisons for alternative models are shown in Figures S2 and S3.[23,24]

Our new model, in addition to fully coupled simulations, successfully predicts experimental data over a wide range of parameters reported by different research groups. A comprehensive summary of the data can be found in Table S1.[39−45] An extensive experimental validation for the new model is shown in Figure 5. Panels a and b present the relative error in ΔG_B prediction from Kowalczyk's model and our new model, respectively, compared to the reported experimental data. The average percentage errors over 44 data points are 36% and 16% for the two models, respectively. It is clear from these figures that the new physics-based approach yields a model that outperforms the existing state-of-the-art models over the complete range of α for thin pores. Moreover, upon comparison of the absolute ΔG_B values in Figure 5c for a particular data set that reports a fairly constant β, the markers for the new model (filled triangles) are much closer to the experimental markers (empty circles) as α is varied, suggesting a better match. Finally, the validity and higher accuracy of the

new model become abundantly clear as the predictions lie close to the parity line ($x = y$) in Figure 5d.

As discussed above, phenomenological parameter θ should be closer to 45° in the ideal scenario in which the equipotential lines conform to the proposed trapezoidal partition between the access and channel regions. However, a closer look at the equipotential lines suggests that the equipotential lines become flat a short distance into the pore mouth. Under this condition, the boundary between the channel and access region would be well represented by a nearly flat (small angle) boundary. As a result, the results are not sensitive to θ in our physics-based model (Figure S6b), which is evaluated as a best-fit parameter using a fourth of the simulation data set. We show that even without an added second-order approximation ($\theta = 0$, i.e., flat equipotential surface), the model (eqs 2−4) outperforms the existing models (Figure S6a). The curvature of the equipotential surface is already accounted for, in part, by eq 2.

In conclusion, the new model serves the need for a more accurate model in the especially critical thin pore limit. It demonstrates the nontrivial dependence of R_{access} on the presence of an analyte and successfully predicts the conductance for a wide range of the experimental data set. Going beyond current applications, the model formulation can be adopted for problems involving any gradient-driven flow such as diffusiophoresis or pressure-driven flows. The general framework for solving the Laplace equation lends the approach its broader applicability. Fundamentally, our approach building on Smythe's work is powerful because it can be extended beyond axisymmetric geometries to systems that admit Schwartz−Cristoffel transformation.[46,47]

We propose a novel partitioning scheme for the nanopore system accounting for the changes in the equipotential surface as a result of analyte translocation through nanopores. A physics-based, more accurate conductance model emerges as a result of the improved system decomposition and capacitance calculations. Certain limitations of the modeling approach, however, such as the effects of heterogeneity in pore shape, salt concentration dependence, and anomalies associated with off-axis translocation[48] will be critical to carefully consider when parsing data from nanopore translocation experiments. The model has been developed for high-salt conditions, where the strength of diffusive fluxes is negligible compared to that of the deterministic migration fluxes caused by the applied electric field. A majority of nanopore measurements are conducted under high-salt conditions to enhance detection sensitivity and signal-to-noise ratio, precisely the conditions under which the new model is expected to perform the best. An implicit assumption in our modeling approach is that the distribution of the electric field lines in a conductive system is the same as that in the analogical dielectric system. The distribution of electric field lines in the vicinity of the pore region mediates the conductance, and the distribution does not change significantly beyond a certain analyte length, l (Figure S7); $l \gg L$ for reported simulation and experimental results. Perhaps any errors from the Poisson−Boltzmann approach at high salt concentrations cancel out the error from the assumption mentioned above. Overall, we expect our modeling framework to become a convenient yet accurate method for conductance estimates for various pore geometries and driving forces in nanopore translocation.

We anticipate that these results can be directly applied in various solid-state nanopore applications, including data storage,[49] profiling polymer topology,[9,10] peptide sequencing,[13]

virus screening, etc. The modeling framework can also be used to improve the accuracy of nanopore base calling in genomic technologies. The state-of-the-art sequencing technologies suffer from high error rates of 5−15%.[50] Such a framework can support model development to overcome these challenges by helping us better understand the signal characteristics as well as for signal calibration and normalization. Accurate conductance models like ours can improve the accuracy and reliability of various single-molecule applications of nanopores.[4]

■ ASSOCIATED CONTENT

Ⓢ Supporting Information

The Supporting Information is available free of charge at https://pubs.acs.org/doi/10.1021/acs.nanolett.3c04997.

> Additional model results and comparison, experimental validation data, methods including analytical model formulation, and simulation model setup (PDF)

■ AUTHOR INFORMATION

Corresponding Author

Patrick S. Doyle − *Department of Chemical Engineering, Massachusetts Institute of Technology, Cambridge, Massachusetts 02142, United States; Singapore-MIT Alliance for Research and Technology Centre, Singapore 138602;* ⓞ orcid.org/0000-0003-2147-9172; Email: pdoyle@mit.edu

Authors

Arjav Shah − *Department of Chemical Engineering, Massachusetts Institute of Technology, Cambridge, Massachusetts 02142, United States; Singapore-MIT Alliance for Research and Technology Centre, Singapore 138602;* ⓞ orcid.org/0000-0002-1531-4470

Shakul Pathak − *Department of Chemical Engineering, Massachusetts Institute of Technology, Cambridge, Massachusetts 02142, United States;* ⓞ orcid.org/0009-0006-3244-1670

Kun Li − *Singapore-MIT Alliance for Research and Technology Centre, Singapore 138602;* ⓞ orcid.org/0009-0009-6190-5640

Slaven Garaj − *Department of Physics, National University of Singapore, Singapore 119077; Singapore-MIT Alliance for Research and Technology Centre, Singapore 138602;* ⓞ orcid.org/0000-0001-5529-4040

Martin Z. Bazant − *Department of Chemical Engineering, Massachusetts Institute of Technology, Cambridge, Massachusetts 02142, United States; Department of Mathematics, Massachusetts Institute of Technology, Cambridge, Massachusetts 02142, United States;* ⓞ orcid.org/0000-0002-8200-4501

Ankur Gupta − *Department of Chemical and Biological Engineering, University of Colorado, Boulder, Colorado 80303, United States;* ⓞ orcid.org/0000-0003-3474-9522

Complete contact information is available at:
https://pubs.acs.org/10.1021/acs.nanolett.3c04997

Author Contributions

A.S., S.G., and P.S.D. conceived the project. A.S. performed the simulations. A.S., S.P., A.G., and P.S.D. analyzed the data. A.S., S.P., M.Z.B., A.G., and P.S.D. developed the analytical model. A.S., S.P., K.L., and S.G. performed the experimental validation. All authors discussed the results and wrote the manuscript. All authors have given approval to the final version of the manuscript.

Notes

The authors declare no competing financial interest.

■ REFERENCES

(1) Deamer, D.; Akeson, M.; Branton, D. Three decades of nanopore sequencing. *Nature Biotechnology 2016 34:5* **2016**, *34*, 518−524.

(2) Ying, Y.-L.; Hu, Z.-L.; Zhang, S.; Qing, Y.; Fragasso, A.; Maglia, G.; Meller, A.; Bayley, H.; Dekker, C.; Long, Y.-T. Nanopore-based technologies beyond DNA sequencing. *Nat. Nanotechnol.* **2022**, *17*, 1136−1146.

(3) Muthukumar, M.; Plesa, C.; Dekker, C. Single-molecule sensing with nanopores. *Phys. Today* **2015**, *68*, 40−46.

(4) Wang, Y.; Zhao, Y.; Bollas, A.; Wang, Y.; Au, K. F. Nanopore sequencing technology, bioinformatics and applications. *Nat. Biotechnol.* **2021**, *39*, 1348−1365.

(5) Heiranian, M.; Farimani, A. B.; Aluru, N. R. Water desalination with a single-layer MoS2 nanopore. *Nat. Commun.* **2015**, *6*, 8616.

(6) Macha, M.; Marion, S.; Nandigana, V. V. R.; Radenovic, A. 2D materials as an emerging platform for nanopore-based power generation. *Nature Reviews Materials* **2019**, *4*, 588−605.

(7) Henrique, F.; Zuk, P. J.; Gupta, A. Charging dynamics of electrical double layers inside a cylindrical pore: predicting the effects of arbitrary pore size. *Soft Matter* **2021**, *18*, 198−213.

(8) Plesa, C.; Verschueren, D.; Pud, S.; van der Torre, J.; Ruitenberg, J. W.; Witteveen, M. J.; Jonsson, M. P.; Grosberg, A. Y.; Rabin, Y.; Dekker, C. Direct observation of DNA knots using a solid-state nanopore. *Nat. Nanotechnol.* **2016**, *11*, 1093−1097.

(9) Kumar Sharma, R.; Agrawal, I.; Dai, L.; Doyle, P. S.; Garaj, S. Complex DNA knots detected with a nanopore sensor. *Nat. Commun.* **2019**, *10*, 4473.

(10) Sharma, R. K.; Agrawal, I.; Dai, L.; Doyle, P. S.; Garaj, S. DNA Knot Malleability in Single-Digit Nanopores. *Nano Lett.* **2021**, *21*, 3772−3779.

(11) Yusko, E. C.; Bruhn, B. R.; Eggenberger, O. M.; Houghtaling, J.; Rollings, R. C.; Walsh, N. C.; Nandivada, S.; Pindrus, M.; Hall, A. R.; Sept, D.; Li, J.; Kalonia, D. S.; Mayer, M. Real-time shape approximation and fingerprinting of single proteins using a nanopore. *Nat. Nanotechnol.* **2017**, *12*, 360−367.

(12) Brinkerhoff, H.; Kang, A. S. W.; Liu, J.; Aksimentiev, A.; Dekker, C. Multiple rereads of single proteins at single−amino acid resolution using nanopores. *Science* **2021**, *374*, 1509−1513.

(13) Alfaro, J. A.; et al. The emerging landscape of single-molecule protein sequencing technologies. *Nat. Methods* **2021**, *18*, 604−617.

(14) Uram, J. D.; Ke, K.; Hunt, A. J.; Mayer, M. Submicrometer pore-based characterization and quantification of antibody-virus interactions. *Small* **2006**, *2*, 967−972.

(15) McMullen, A.; de Haan, H. W.; Tang, J. X.; Stein, D. Stiff filamentous virus translocations through solid-state nanopores. *Nat. Commun.* **2014**, *5*, 4171.

(16) Li, K.; Shah, A.; Sharma, R. K.; Adkins, R.; Marjanovic, T.; Doyle, P. S.; Garaj, S. Metrology of individual small viruses. *Adv. Mater. Interfaces* **2023**, *10*, No. 2300385.

(17) Taniguchi, M.; et al. Combining machine learning and nanopore construction creates an artificial intelligence nanopore for coronavirus detection. *Nat. Commun.* **2021**, *12*, 3726.

(18) Kasianowicz, J.; Brandin, E.; Branton, D.; Deamer, D. Characterization of individual polynucleotide molecules using a membrane channel. *Proc. Natl. Acad. Sci. U. S. A.* **1996**, *93*, 13770−13773.

(19) Wu, H.; Chen, Y.; Zhou, Q.; Wang, R.; Xia, B.; Ma, D.; Luo, K.; Liu, Q. Translocation of Rigid Rod-Shaped Virus through Various Solid-State Nanopores. *Anal. Chem.* **2016**, *88*, 2502−2510.

(20) Qiao, L.; Slater, G. W. Capture of rod-like molecules by a nanopore: Defining an "orientational capture radius. *J. Chem. Phys.* **2020**, *152*, No. 144902.

(21) Venta, K. E.; Zanjani, M. B.; Ye, X.; Danda, G.; Murray, C. B.; Lukes, J. R.; Drndić, M. Gold Nanorod Translocations and Charge Measurement through Solid-State Nanopores. *Nano Lett.* **2014**, *14*, 5358−5364.

(22) He, L.; Charron, M.; Mensing, P.; Briggs, K.; Adams, J.; de Haan, H.; Tabard-Cossa, V. DNA origami characterized via a solid-state nanopore: insights into nanostructure dimensions, rigidity and yield. *Nanoscale* **2023**, *15*, 14043−14054.

(23) Kowalczyk, S. W.; Grosberg, A. Y.; Rabin, Y.; Dekker, C. Modeling the conductance and DNA blockade of solid-state nanopores. *Nanotechnology* **2011**, *22*, No. 315101.

(24) Carlsen, A. T.; Zahid, O. K.; Ruzicka, J.; Taylor, E. W.; Hall, A. R. Interpreting the conductance blockades of DNA translocations through solid-state nanopores. *ACS Nano* **2014**, *8*, 4754−4760.

(25) Tang, W.; Fried, J. P.; Tilley, R. D.; Gooding, J. J. Understanding and modelling the magnitude of the change in current of nanopore sensors. *Chem. Soc. Rev.* **2022**, *51*, 5757−5776.

(26) Arjmandi-Tash, H.; Belyaeva, L. A.; Schneider, G. F. Single molecule detection with graphene and other two-dimensional materials: nanopores and beyond. *Chem. Soc. Rev.* **2016**, *45*, 476−493.

(27) Danda, G.; Drndić, M. Two-dimensional nanopores and nanoporous membranes for ion and molecule transport. *Curr. Opin. Biotechnol.* **2019**, *55*, 124−133.

(28) Maxwell, J. C. *A treatise on electricity and magnetism*; Clarendon: Oxford, U.K., 1881; Vol. *314*, p 1873.

(29) Hille, B. Pharmacological Modifications of the Sodium Channels of Frog Nerve. *J. Gen. Physiol.* **1968**, *51*, 199−219.

(30) Hall, J. E. Access resistance of a small circular pore. *J. Gen. Physiol.* **1975**, *66*, 531−532.

(31) Wexler, J. S.; Trinh, P. H.; Berthet, H.; Quennouz, N.; du Roure, O.; Huppert, H. E.; Lindner, A.; Stone, H. A. Bending of elastic fibres in viscous flows: the influence of confinement. *J. Fluid Mech.* **2013**, *720*, 517−544.

(32) Atwal, H. K.; Wong, A. O. K.; Boutilier, M. S. H. Mass Advection−Diffusion in Creeping Flow Through an Orifice Plate: A Model for Nanoporous Atomically Thin Membranes. *J. Heat Transfer* **2022**, *144* (2), 022701.

(33) Bazant, M. Z.; Kilic, M. S.; Storey, B. D.; Ajdari, A. Towards an understanding of induced-charge electrokinetics at large applied voltages in concentrated solutions. *Adv. Colloid Interface Sci.* **2009**, *152*, 48−88.

(34) Smith, A. M.; Lee, A. A.; Perkin, S. The Electrostatic Screening Length in Concentrated Electrolytes Increases with Concentration. *J. Phys. Chem. Lett.* **2016**, *7*, 2157−2163.

(35) Li, H.-K.; Pedro de Souza, J.; Zhang, Z.; Martis, J.; Sendgikoski, K.; Cumings, J.; Bazant, M. Z.; Majumdar, A. Imaging Arrangements of Discrete Ions at Liquid−Solid Interfaces. *Nano Lett.* **2020**, *20*, 7927−7932.

(36) Olver, P. J. Complex Analysis and Conformal Mapping. University of Minnesota, 2017, 806.

(37) Smythe, W. R. The Capacitance of a Circular Annulus. *J. Appl. Phys.* **1951**, *22*, 1499−1501.

(38) Smythe, W. B. *Static and dynamic electricity*, 3rd ed.; 1988.

(39) Garaj, S.; Hubbard, W.; Reina, A.; Kong, J.; Branton, D.; Golovchenko, J. A. Graphene as a subnanometre trans-electrode membrane. *Nature* **2010**, *467*, 190−193.

(40) Garaj, S.; Liu, S.; Golovchenko, J. A.; Branton, D. Molecule-hugging graphene nanopores. *Proc. Natl. Acad. Sci. U.S.A.* **2013**, *110*, 12192−12196.

(41) Liu, S.; Lu, B.; Zhao, Q.; Li, J.; Gao, T.; Chen, Y.; Zhang, Y.; Liu, Z.; Fan, Z.; Yang, F.; You, L.; Yu, D. Boron Nitride Nanopores: Highly Sensitive DNA Single-Molecule Detectors. *Adv. Mater.* **2013**, *25*, 4549−4554.

(42) Wang, L.; Boutilier, M. S. H.; Kidambi, P. R.; Jang, D.; Hadjiconstantinou, N. G.; Karnik, R. Fundamental transport mechanisms, fabrication and potential applications of nanoporous atomically thin membranes. *Nat. Nanotechnol.* **2017**, *12*, 509−522.

(43) Merchant, C. A.; Healy, K.; Wanunu, M.; Ray, V.; Peterman, N.; Bartel, J.; Fischbein, M. D.; Venta, K.; Luo, Z.; Johnson, A. T. C.; Drndić, M. DNA Translocation through Graphene Nanopores. *Nano Lett.* **2010**, *10*, 2915−2921.

(44) Rodríguez-Manzo, J. A.; Puster, M.; Nicolaï, A.; Meunier, V.; Drndić, M. DNA Translocation in Nanometer Thick Silicon Nanopores. *ACS Nano* **2015**, *9*, 6555−6564.

(45) Schneider, G. F.; Kowalczyk, S. W.; Calado, V. E.; Pandraud, G.; Zandbergen, H. W.; Vandersypen, L. M. K.; Dekker, C. DNA Translocation through Graphene Nanopores. *Nano Lett.* **2010**, *10*, 3163−3167.

(46) Driscoll, T. A.; Trefethen, L. N. *Schwarz-Christoffel Mapping*; Cambridge University Press, 2002; Vol. *8*.

(47) Bazant, M. Z. Conformal Mapping of Some Non-Harmonic Functions in Transport Theory. *Proceedings: Mathematical, Physical and Engineering Sciences* **2004**, *460*, 1433−1452.

(48) Ying, C.; Houghtaling, J.; Mayer, M. Effects of off-axis translocation through nanopores on the determination of shape and volume estimates for individual particles. *Nanotechnology* **2022**, *33*, No. 275501.

(49) Chen, K.; Zhu, J.; Bošković, F.; Keyser, U. F. Nanopore-Based DNA Hard Drives for Rewritable and Secure Data Storage. *Nano Lett.* **2020**, *20*, 3754−3760.

(50) Rang, F. J.; Kloosterman, W. P.; de Ridder, J. From squiggle to basepair: computational approaches for improving nanopore sequencing read accuracy. *Genome Biol.* **2018**, *19*, 90.